COMPUTER METHODS IN MATERIALS SCIENCE

2026, vol. 26, no. 1, 23–42
https://doi.org/10.7494/cmms.2026.1.1038

Geometric optimization of two-stage stamping dies for ultra-thin titanium bipolar plates using Sequential Physics-Informed Neural Networks

Zijie Ke[1], Yiwen Huang[1], Ziqiang Guo[1], Yao Xiao[1]*, Zeran Hou[1], Junying Min[2]

[1] School of Mechanical Engineering, Tongji University, Shanghai 201804, China.
[2] College of Automotive and Energy Engineering, Tongji University, Shanghai 201804, China.

Abstract

Bipolar plates are critical core components in proton exchange membrane fuel cells (PEMFCs). Titanium-based materials are highly favored due to their excellent corrosion resistance and high specific strength. However, the plates often experience severe local thinning and poor consistency in forming dimensions during the two-stage stamping process. Although traditional finite element method (FEM) optimization can mitigate these defects, it comes with high computational costs and time consumption. This study proposes a die design optimization framework based on the Sequential Physics-Informed Neural Network (S-PINN). Unlike traditional single-layer neural network models, S-PINN adopts a sequential architecture that effectively maps the two-stage forming process of the plates. This architecture can explicitly predict the evolution of forming quality from the pre-forming stage to the final stage. By embedding the core physical laws of plastic deformation into the network loss function, the S-PINN model effectively predicts the complex nonlinear relationship between mold geometry and forming quality, while ensuring physical consistency. Experimental and simulation results show that the S-PINN model's prediction accuracy for dimensional consistency (*DC*) is 73.8% higher than that of the PINN model and 33.9% higher than that of the S-ANN model. Compared with traditional modeling methods, the S-PINN-optimized die design can reduce the thinning rate and improve channel dimensional consistency.

Keywords: Sequential Physics-Informed Neural Network, ultra-thin titanium sheet, two-stage forming, die shape optimization, thinning rate, dimensional consistency

1. Introduction

With the urgency of global climate change and the demand for carbon neutrality, proton exchange membrane fuel cells (PEMFCs) are undergoing rapid development (Heras et al., 2009; Daud et al., 2017). As a key component of the PEMFC stack, the bipolar plate simultaneously functions as a gas separator, conductor, coolant channel, and load-bearing element (Bong et al., 2017). Its weight accounts for approximately 80% of the total stack weight, and its manufacturing cost accounts for 40%. Among various bipolar plate materials, titanium alloy metal bipolar plates have attracted significant attention in the industry. As a high-quality metal, titanium's

* Corresponding author
Authors' e-mails: 2330399@tongji.edu.cn, 2330391@tongji.edu.cn, 2430515@tongji.edu.cn, xiaoy10@tongji.edu.cn, zeranhou@tongji.edu.cn, junying.min@tongji.edu.cn
ORCID IDs: 0009-0009-4666-0438 (Z. Ke), 0009-0001-7006-147X (Y. Huang), 0009-0001-1891-2812 (Z. Guo), 0000-0003-3011-8408 (Y. Xiao), 0000-0003-4060-6317 (Z. Hou), 0000-0002-1754-6259 (J. Min)
Received: 6.03.2026, accepted: 13.04.2026, published: 29.04.2026

excellent strength-to-weight ratio and outstanding corrosion resistance make it an ideal candidate material for the new generation of compact fuel cells (Lin et al., 2023).

Although titanium has inherent material advantages (Bajda & Krzyzanowski, 2019), its forming process faces significant challenges. Efficient gas distribution requires extremely high accuracy in plate channel dimensions and aspect ratios. This complex geometric structure is prone to defects during manufacturing, such as local thinning at channel corners and severe springback during plate forming. Excessive thinning can compromise the mechanical integrity of the plate, leading to cracking and corrosion penetration. Moreover, inconsistent plate dimensions can result in uneven contact pressure with the gas diffusion layer, causing local hot spots and sharply increasing the contact resistance, ultimately significantly reducing the overall efficiency of the fuel cells. Currently, the industry widely employs advanced process strategies such as two-stage stamping to alleviate manufacturing defects and extend the forming limits of bipolar plates (Bong et al., 2017; Zhang R. et al., 2021). However, such multi-stage manufacturing processes also increase the complexity of stamping die design.

Traditional stamping die optimization mainly relies on trial-and-error methods or rigorous finite element methods (FEM) (Zhong et al., 2023). These traditional approaches face computational bottlenecks when handling iterative optimization tasks, characterized by long time consumption and high costs. To address this challenge, researchers widely adopt surrogate-based optimization (SBO) methods (Han & Zhang, 2012). Among these, the response surface method (RSM) (Bezerra et al., 2008) and kriging (Gaussian process) (Oliver & Webster, 1990) are two typical surrogate models. They are extensively used to fit parameter relationships and approximately describe the interactions between design variables and performance indicators. However, these traditional data-driven models are essentially invisible "black boxes." They rely entirely on statistical correlations within the training dataset, thereby neglecting the physical principles governing the plastic deformation process. Therefore, to ensure predictive accuracy, such models usually require massive datasets, significantly prolonging the cycle of die structure optimization.

In recent years, neural networks have been widely applied in the field of process optimization of sheet metal forming. Alhalaybeh et al. (2026) proposed a framework for forming process parameter optimization based on artificial neural networks (ANN) in this field. By establishing a mapping relationship between geometric parameters and forming quality, this method effectively optimized specific forming processes. Xiao et al. (2022), on the other hand, took a different approach and developed a new multi-objective optimization algorithm that deeply integrates the response surface method with evolutionary algorithms, successfully achieving the synergistic control of springback and thinning rate in microchannel stamping. However, these models rely entirely on pure statistical fitting and are not strictly constrained by physical laws. When faced with complex intermediate deformation paths or unknown extrapolation scenarios, such models often produce predictions that defy physical intuition, severely limiting the ability of traditional neural networks in engineering practice to generalize. To overcome the inherent limitations of purely data-driven models, Physics-Informed Neural Networks (PINNs) emerged. By embedding physical laws into the machine learning process, this technology provides a new paradigm for solving complex nonlinear engineering problems. Raissi et al. (2019) made breakthrough progress by proposing a deep learning framework that integrates physical knowledge. They embedded partial differential equations (PDEs) as physical rules into neural networks, directly coupling PDE residuals through the loss function, thereby achieving both forward solving of nonlinear PDEs and parameter inversion simultaneously. On this basis, Karniadakis et al. (2021) significantly expanded the application range of PINNs by using physical conservation laws to guide neural network weight updates, greatly enhancing model robustness in sparse data environments. Similarly, Haghighat et al. (2021) introduced physics-driven deep learning into the field of solid mechanics, effectively ensuring the physical rationality of output data by penalizing predictions that contradict continuum mechanics. Although PINNs and their variants have enormous potential in engineering, directly applying them to multi-stage micro-stamping processes still faces significant challenges. The two-stage forming process of ultra-thin titanium bipolar plates involves complex path dependency and irreversible plastic damage. Standard PINN models struggle to accurately capture and quantify the interactions between different forming stages in such processes, often simplifying multi-stage forming into a single system, resulting in over-simplification of the problem.

To address these challenges, this paper proposes a new die geometry optimization framework for the two-stage stamping process of ultra-thin titanium plates. This paper proposes a Sequential Physics-Informed Neural Networks (S-PINN) framework that sequentially decomposes the entire two-stage stamping process and introduces a monotonic residual term into the loss function. This residual term enforces the irreversibility of plastic damage mathematically, enabling the model to learn the logical relationships between forming stages while fully considering the impact of the pre-forming process on the final forming state. In addition, to comprehensively as-

sess the model prediction accuracy, this paper introduces two key indicators: Root Mean Square Error (RMSE) and fractional error. These indicators can evaluate the accuracy and limitations of the Physics-Informed Neural Network (PINN), Sequential Artificial Neural Network (S-ANN), and Sequential Physics-Informed Neural Network (S-PINN) models.

2. Materials & methods

2.1. Material properties characterization and stamping experiments

This study selected commercial pure titanium sheets with a thickness of 0.12 mm (Song et al., 2020), whose main chemical compositions are: titanium (99.50%), sodium (0.23%), magnesium (0.08%), iron (0.04%), nickel (0.02%), and silicon (0.02%). Uniaxial tensile tests were conducted along different orientations of the base material to accurately characterize the mechanical properties of commercial CP-Ti sheets. The uniaxial tensile test procedures were highly standardized, and the entire testing process strictly followed the GB/T 228-2002 standard. Test specimens were cut along three different angles: rolling direction (RD), diagonal direction (DD), and transverse direction (TD), to prepare standard tensile specimens with a gauge section of 12.5 mm × 75.0 mm. All tests were carried out at room temperature, with a constant crosshead displacement rate of 0.01 mm/s, corresponding to a nominal strain rate of 1.33×10^{-4} s^{-1}. The true stress-strain curve of the material is shown in Fig. 1a. Other detailed mechanical property parameters are listed in Tab. 1.

Table 1. Mechanical properties for CP-Ti

Orientation	Elastic modulus [GPa]	Yield strength [MPa]	Tensile strength [MPa]	*r*-value
RD	93.30	196.53	320.30	1.66
DD	97.10	204.84	292.69	3.89
TD	105.40	215.42	309.58	5.68

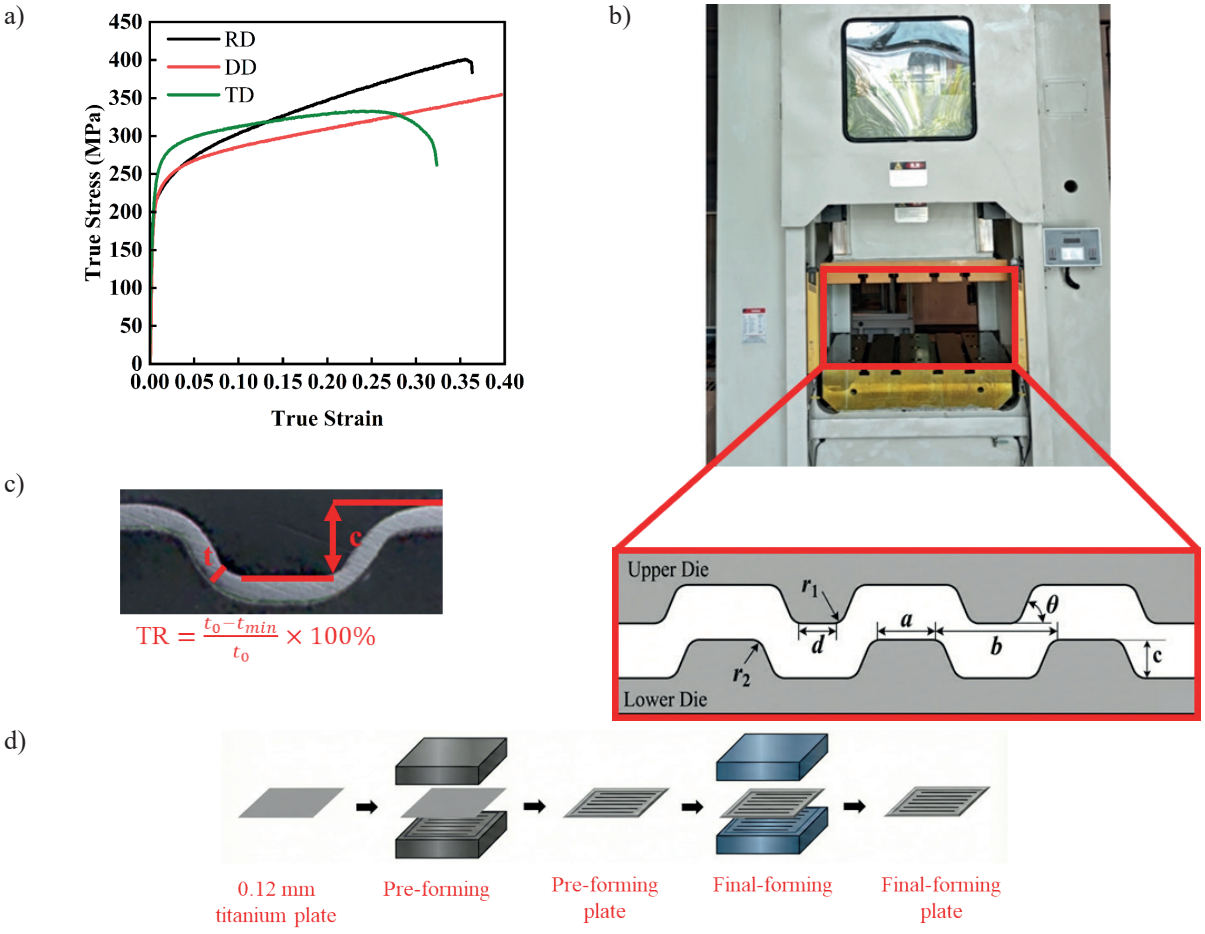

Fig. 1. Material properties and experimental setup for the stamping process: a) true stress-strain curves for the CP-Ti material in the RD, DD, and TD; b) equipment setup using a Yadon 630 press, with an inset detailing the geometric parameters of the forming dies; c) optical micrograph of the channel cross-section defining the geometric characteristics and the thinning rate (*TR*); d) schematic illustration of the two-stage forming procedure for the titanium bipolar plate

The stamping dies used in the experiment were all made of high-strength H13 hot-work tool steel. The specific geometric parameters of the dies are shown in the schematic in Fig. 1b, mainly including the rib width (a), groove width (d), and draft angle (β). The die structure also includes the top corner radius (r_1), bottom corner radius (r_2), and key groove depth (c). Accordingly, the channel period (pe) is always maintained at a constant value of 1.5 mm. Due to the geometric constraints of the die, only five of the six mold parameters are needed to obtain the value of the last parameter, which satisfies Eq. (1):

$$(1-\cos\beta)(r_1+r_2)+\frac{1}{2}\tan\beta(pe|a|d)- (r_1+r_2)\sin\beta\tan\beta=c \quad (1)$$

The experiment used rectangular blanks measuring 128 × 78 mm². As shown in Fig. 1d, the experimental process consists of four separate stages: (a) the first-stage stamping using the initial forming die; (b) springback caused by stress release after die reset; (c) the second-stage stamping using the subsequent forming die; (d) final springback after die reset.

After the forming process was completed, the samples were air-cooled for 30 minutes to ensure thermal equilibrium. The formed sheets were cleaned and fixed in a jig for geometric inspection, and the cross-sectional profiles were measured using a high-precision optical microscope with a resolution of up to 0.001 mm (Fig. 1c). In the optimization study, two core quality indicators were defined as target variables:

1. Thinning rate (TR): This indicator identifies the most severe thinning in the sheet thickness direction, which usually occurs in regions of stress concentration (especially at channel corners), with the calculation formula shown in Fig. 1c.
2. Dimensional consistency (DC): Defined as the deviation between the maximum and minimum channel depths observed on the formed sheet, reflecting the uniformity of stamping quality.

2.2. Finite element analysis (FEA)

The two-stage stamping process was numerically simulated using the Abaqus/Explicit (2022) dynamic solver. The finite element model employed is shown in Fig. 2a. The sheet metal has a thickness of 0.12 mm and a width of 0.50 mm. This 0.5 mm width acts as a standard plane-strain simplification. Because bipolar plate channels are long and parallel, the material flow parallel to the channels is negligible compared to the transverse drawing and bending, allowing this simplification to save massive computational costs while accurately capturing the cross-sectional thinning and dimensional consistency (Modanloo et al., 2025). It was divided into four distinct element layers along the thickness direction, comprising 34,844 C3D8R meshes. Local mesh refinement was applied in the stress concentration zones to ensure at least three solid elements spanned the die fillet. The die was modeled using an R3D4 rigid mesh, as shown in Fig. 2b, with local mesh refinement also applied at the die fillet.

In the finite element simulation, both the upper and lower dies are modeled as analytically rigid surfaces, with die deformation considered negligible. The interaction between the sheet metal and the dies is defined using the surface-to-surface contact formula within the general contact algorithm. The die surfaces are designated as primary surfaces, while the sheet metal surfaces are treated as secondary surfaces.

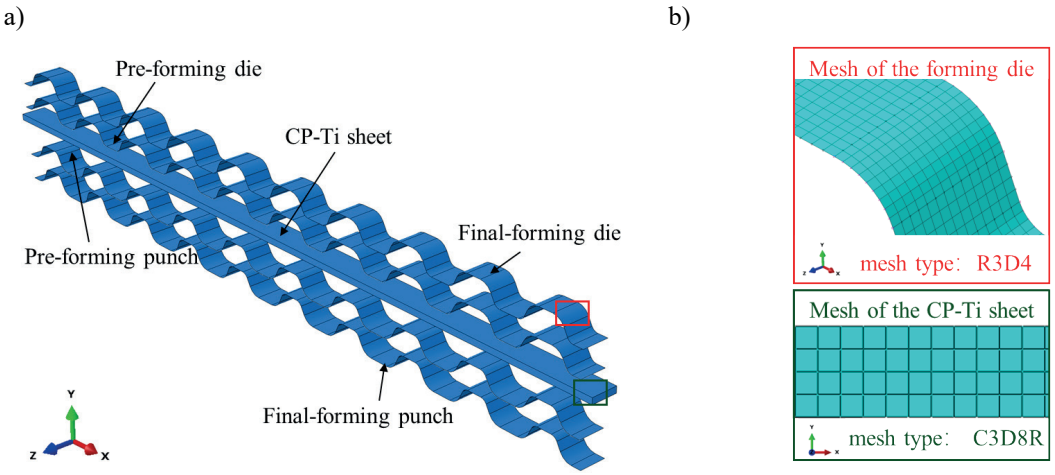

Fig. 2. Finite element model for the two-stage stamping process: a) 3D schematic of the preform dies, ultra-thin CP-Ti plate, and final forming dies; b) localized enlargement of the sheet metal and die mesh

A friction model based on a penalty term is employed, with a constant friction coefficient of 0.125 set to simulate the contact conditions. This value is determined based on existing literature and experimental calibration of lubricated cold stamping of commercial pure titanium (CP-Ti) sheets (Guo et al., 2023). To enhance the computational efficiency while maintaining the validity of the quasi-static assumption, a 1000-fold mass scaling factor is applied.

The plastic deformation behavior of commercial purity titanium (CP-Ti) sheet was characterized using the Hill48 yield criterion, which accounts for planar anisotropy in the material (Yan et al., 2015). Strain hardening behavior was modeled through a modified Hockett–Sherby (H–S) constitutive relationship (Eq. (2)) (Zhang H. et al., 2023), incorporating an associative flow rule.

$$\bar{\sigma}(\bar{\varepsilon}_p) = \sigma_{sat} - (\sigma_{sat} - \sigma_y)\exp(-m\bar{\varepsilon}_p^n) + p\bar{\varepsilon}_p^k \qquad (2)$$

where: $\bar{\sigma}$ – equivalent flow stress; $\bar{\varepsilon}_p$ – plastic equivalent strain; σ_y – the initial yield stress; σ_{sat} – saturation stress; m, n, p, k – material parameters (as shown in Tab. 2).

The accuracy of the FEA can be found in Appendix A.

Table 2. Input parameters of constitutive model

r_0	r_{45}	r_{90}	σ_{sat}	σ_y	m	n	p	k
1.36	3.89	5.68	415.78	220.52	6.42	0.71	17.40	16.37

During the dynamic simulation process, Abaqus/Explicit was utilized to simulate the dynamic stamping stroke. Because explicit algorithms can encounter dynamic oscillation errors during springback prediction, the deformed mesh with residual stresses was subsequently imported into Abaqus/Standard for the springback calculations. To ensure the reliability of the surrogate model, the baseline FEM model was systematically validated against experimental data. The simulated cross-sectional profile of a baseline die design was compared against the experimental optical micrographs, confirming the fidelity of the ground-truth data used for training. A total of 500 FEA simulation cases were conducted to generate the comprehensive dataset.

2.3. S-PINN model

In two-stage stamping processes, the material's forming state depends not only on the final forming operation but also on the strain history accumulated during the preforming stage. Traditional artificial neural networks (ANNs) (Yang, 2008; Lacki et al., 2026) typically map input design variables directly to final performance metrics. This computationally simplified approach treats multi-stage manufacturing sequences as single input-output operations, essentially ignoring the cumulative plastic deformation process of the workpiece.

To overcome this limitation, this study proposes a novel Sequential Physics-Informed Neural Network (S-PINN) framework based on the basic principles of an ANN. Unlike a standard single network architecture, S-PINN employs a sequential structure design to accurately map the two-stage stamping process, as shown in Fig. 3. It explicitly predicts the preforming results through a dedicated neural network and uses them as a prerequisite for the final state prediction. This sequential decomposition strategy not only enhances the interpretability of the model, allowing for analysis of the quality of the preformed parts, but also provides key points for injecting intermediate physical constraints, thereby ensuring that the predicted evolution process of the bipolar plates follows the fundamental laws of plastic damage accumulation.

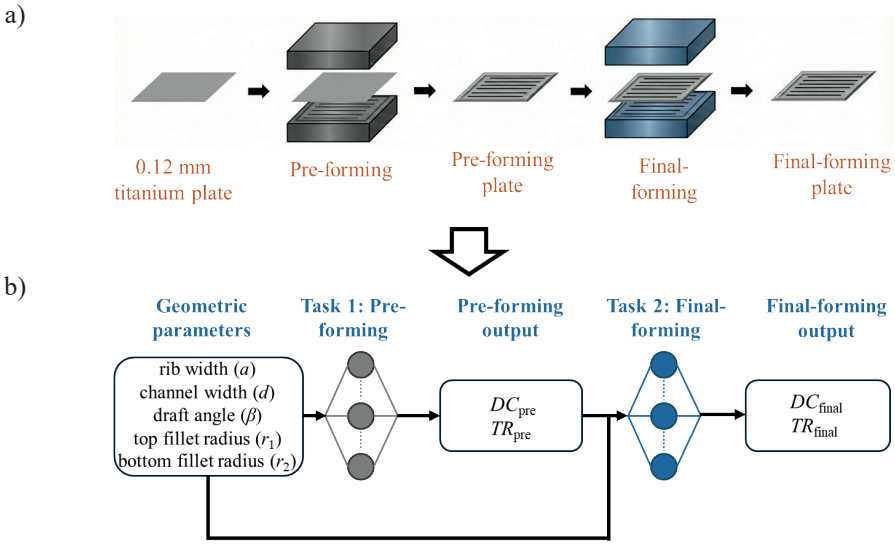

Fig. 3. Schematic representation of the two-stage stamping process: the manufacturing sequence (a) is structurally mapped to a sequential neural network architecture (b)

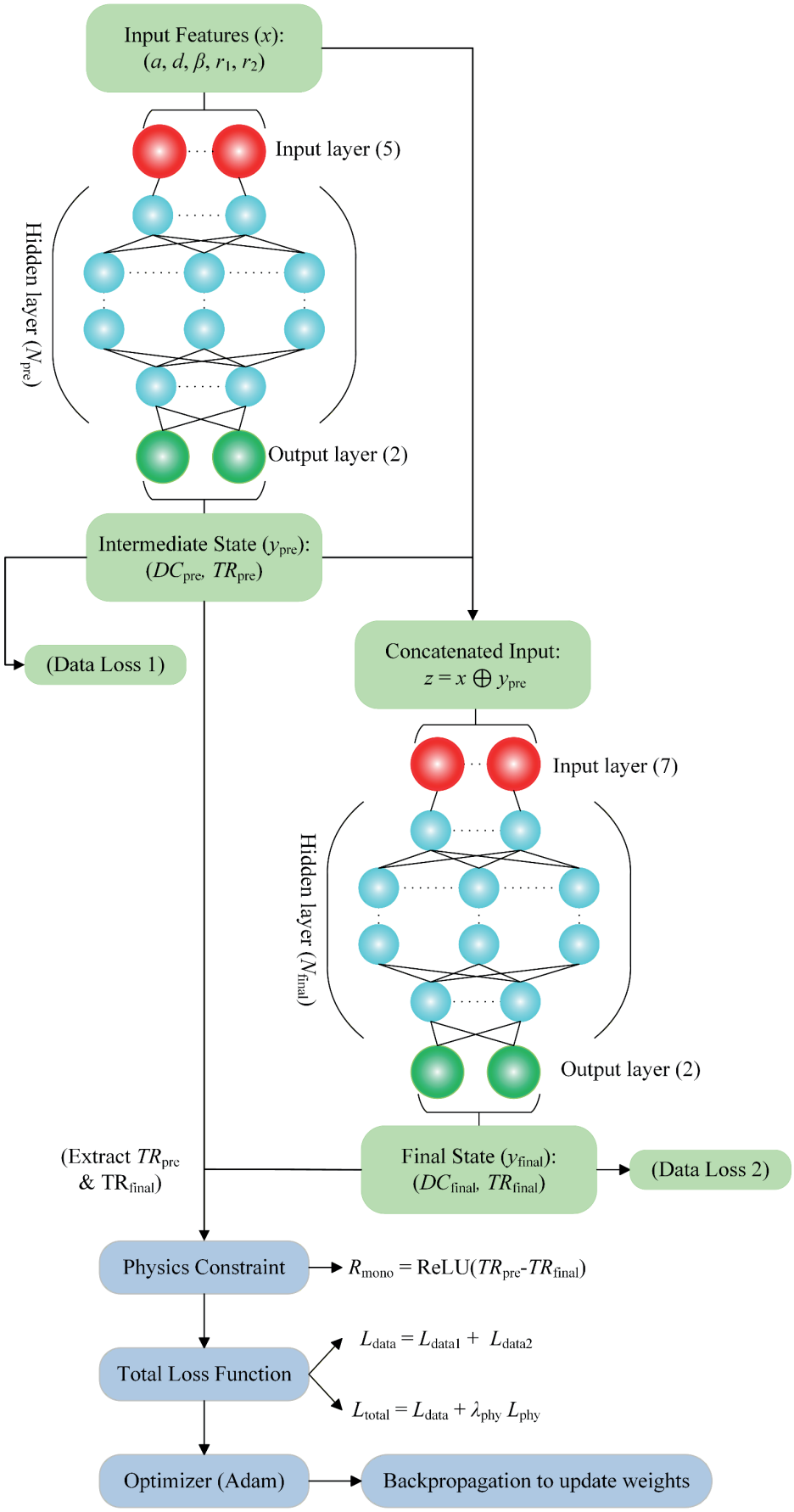

Fig. 4. Detailed architecture of the proposed Sequential Physics-Informed Neural Network (S-PINN)

The S-PINN framework (Fig. 4) is constructed from two fully connected feed-forward Artificial Neural Networks, denoted as the Pre-forming ANN ($\mathcal{N}_{pre}$) and the Final-forming ANN ($\mathcal{N}_{final}$), connected in series. The mathematical formulation and topological structure of these sub-networks are defined as follows:

The pre-forming ANN ($\mathcal{N}_{pre}$) maps the initial die geometric parameters to the forming quality indicators of the pre-forming stage. Let the input vector be denoted by $\boldsymbol{x} \in \mathbb{R}^5$, representing the five key die design variables defined in Section 2.1: rib width (a), groove width (d), draft angle (β), top fillet radius (r_1), and bottom fillet radius (r_2).The network processes this input through a series of hidden layers to predict the intermediate state vector $\boldsymbol{y}_{pre} \in \mathbb{R}^2$. The mapping function is expressed as:

$$\boldsymbol{y}_{pre} = \mathcal{N}_{pre}(\boldsymbol{x}; \boldsymbol{\theta}_{pre}) = [DC_{pre}, TR_{pre}]^T \tag{3}$$

where $\boldsymbol{\theta}_{pre}$ represents the trainable weights and biases of $\mathcal{N}_{pre}$.

The output variables are defined as the dimensional consistency (DC_{pre}) and the thinning rate (TR_{pre}) achieved after the first stamping stroke. Structurally, $\mathcal{N}_{pre}$ consists of multiple hidden layers employing the hyperbolic tangent (tanh) activation function (Fan, 2000).

The final-forming ANN ($\mathcal{N}_{final}$) predicts the quality metrics of the finished product. The input to $\mathcal{N}_{final}$ is not limited to the output of the previous stage (y_{pre}); instead, it is an augmented vector $z \in \mathbb{R}^7$ formed by concatenating the original design parameters x with the intermediate state y_{pre}:

$$z = x \oplus y_{pre} = [a, d, \beta, r_1, r_2, DC_{pre}, TR_{pre}]^T \tag{4}$$

This design is physically motivated by the fact that the final deformation is driven by the interaction between the pre-formed geometry and the final die constraints. The mapping for the second stage is thus:

$$y_{final} = \mathcal{N}_{final}(z; \theta_{final}) = [DC_{final}, TR_{final}]^T \tag{5}$$

where the output vector y_{final} comprises the final dimensional consistency (DC_{final}) and the final thinning rate (TR_{final}).

Similar to the first stage, $\mathcal{N}_{final}$ uses a multilayer perceptron (MLP) architecture to ensure sufficient capacity to capture the complex nonlinear features of the final forming stage.

Purely data-driven artificial neural networks have fundamental limitations: when extrapolating in unknown regions of the design space, their models often violate physical laws. To endow S-PINN with physical intelligence, we introduce a constraint based on the irreversibility of plastic deformation. During the cold stamping process of ultra-thin titanium sheets, the material undergoes plastic flow and local thinning. According to the law of conservation of mass and the principles of plastic mechanics, once the local thickness of the sheet is reduced, it cannot spontaneously recover or "heal" in subsequent forming stages unless a specific compressive force is applied (which does not exist in this process). Therefore, the thinning rate observed in the final component (TR_{final}) must physically be greater than or equal to the thinning rate before forming (TR_{pre}). The mathematical definition of this inequality constraint is:

$$TR_{final}(x) \geq TR_{pre}(x), \forall x \in \Omega \tag{6}$$

where Ω represents the entire design space.

To enforce this physical law during training, a specific monotonicity residual (R_{mono}) is formulated using a rectified linear unit (ReLU) function:

$$R_{mono} = \mathrm{ReLU}\,(TR_{pre} - TR_{final}) \tag{7}$$

The principle of this residual is defined as follows: If the ANN predicts a physically valid scenario where $TR_{final} \geq TR_{pre}$, then ($TR_{pre} - TR_{final}$) is negative or zero and the ReLU function returns 0 (no penalty). However, if the ANN prediction violates the laws of physics, the ReLU function will return the positive magnitude of that error and then add it to the total loss to penalize the model. This mechanism forces the neural network to learn the physical laws of damage accumulation and guide the optimization trajectory in a physically reasonable direction.

The training of the S-PINN is treated as a multi-objective optimization problem where the goal is to simultaneously minimize the prediction error against the ground truth data (from experiments and FEA) and the violation of physical constraints. The total loss function, $\mathcal{L}_{total}$, is defined as a weighted sum of the data-driven loss ($\mathcal{L}_{data}$) and the physics-based loss ($\mathcal{L}_{phy}$):

$$\mathcal{L}_{total} = \mathcal{L}_{data} + \lambda_{phy}\mathcal{L}_{phy} \tag{8}$$

The data-driven loss component, $\mathcal{L}_{data}$, quantifies the discrepancy between the ANN predictions and the labeled dataset generated in Section 2.2. It is calculated using the Mean Squared Error (MSE), aggregated over both forming stages:

$$\mathcal{L}_{data} = \frac{1}{N}\sum_{i=1}^{N}(\lambda_1 \left\| y_{pre}^{(i)} - \hat{y}_{pre}^{(i)} \right\|^2 + \lambda_2 \left\| y_{final}^{(i)} - \hat{y}_{final}^{(i)} \right\|^2) \tag{9}$$

where: N – number of training samples; $y^{(i)}$ – ground truth values; $\hat{y}^{(i)}$ – S-PINN predictions. fig

The coefficients λ_1 and λ_2 are weights assigned to the pre-forming and final-forming tasks, respectively, typically set to 1.0 to treat both stages with equal importance.

The physics-based loss component, $\mathcal{L}_{phy}$, is derived from the monotonicity residual, defined as:

$$\mathcal{L}_{phy} = \frac{1}{N}\sum_{i=1}^{N}\left\|R_{mono}^{(i)}\right\|^2 \tag{10}$$

where $\mathcal{L}_{\text{phy}}$ serves as a regularization hyperparameter that controls the strictness of the physical constraint.

A dynamic weighting strategy was employed during training: initially, $\mathcal{L}_{\text{phy}}$ is set to a low value to allow the ANNs to learn the primary data trends, and is progressively increased to strictly enforce physical consistency as the training converges.

2.4. Baseline model architectures and ablation strategy

In order to systematically evaluate the effectiveness of the proposed computational framework and conduct rigorous ablation studies, this paper constructs and compares three different neural network architectures, with their overall topologies and information flows shown in Fig. 5.

The first benchmark model is the standard Physics-Informed Neural Network (PINN). This traditional architecture establishes a direct mapping from input parameters, including mold geometry parameters and preforming state, to final forming quality indicators. The model takes mold geometry parameters as input and relies on a physics-based loss function to constrain the final output.

To isolate and independently verify the actual effect of physical constraints, this paper introduces a purely data-driven Sequential Artificial Neural Network (S-ANN) as the second benchmark model. Its internal multi-stage topology accurately maps the actual multi-step physical manufacturing process by concatenating the preforming training stage with the final forming training stage. However, the training of the S-ANN relies entirely on fitting statistical data and lacks loss constraints from physical information. Therefore, when facing extrapolation predictions in unknown design spaces, it is difficult to avoid results that violate physical intuition.

Finally, the proposed Sequential Physics-Informed Neural Network (S-PINN) effectively combines the dual advantages of the above two benchmark models in terms of structure and physical constraints. This framework deeply integrates the explicit sequential structural mapping with embedded physical loss constraints. This comprehensive design not only ensures that the model can accurately capture the path-dependency characteristics in the two-stage stamping process but also strictly guarantees that all predicted results comply with the fundamental physical laws of plastic damage accumulation.

2.5. Data processing and feature selection

The S-PINN framework and associated computational algorithms were implemented using the PyTorch deep learning library within a Python 3.12 environment. All numerical experiments were performed on a high-performance workstation equipped with an Intel Core Ultra 7 255H CPU and 32 GB of RAM to ensure computational efficiency.

In the field of machine learning, the quality of a dataset is a critical factor influencing a model's predictive capability. To accelerate model convergence and enhance stability, data normalization is performed using min–max normalization, which can be expressed as (Henderi et al., 2021):

$$x' = \frac{x - x_{\min}}{x_{\max} - x_{\min}} \tag{11}$$

where: x' – normalized value; x_{min}, x_{max} – minimum and maximum values of specific parameters in the training dataset, respectively.

To ensure the scientific rigor and reliability of the machine learning model training and evaluation process, a dataset splitting strategy is used to handle experimental data. The complete dataset (consisting of $N = 500$ samples) is divided into a training set and an independent test set at a fixed ratio of 8 : 2. The training subset, accounting for 80% of the total data, is used for model parameter optimization and learning the physical laws of the stamping process, while the remaining 20% serves as an unseen test set to validate the model's accuracy and resistance to overfitting. The Pearson correlation coefficient (PCC) is used to quantify the linear dependency between die geometric parameters and the target variable. This statistical metric effectively filters the input space by highlighting features associated with forming outcomes. The correlation coefficient ρ is defined as the covariance of variables X and Y divided by the product of their standard deviations (Asuero et al., 2006):

$$\rho_{X,Y} = \frac{\operatorname{cov}(X,Y)}{\sigma_X \sigma_Y} = \frac{E\left[(X-\mu_X)(Y-\mu_Y)\right]}{\sigma_X \sigma_Y} \tag{12}$$

For empirical data, the sample Pearson correlation coefficient, r, is estimated using Eq. (13) (Benesty et al., 2009):

$$r = \frac{\sum_{i=1}^{n}(X_i - \bar{X})(Y_i - \bar{Y})}{\sqrt{\sum_{i=1}^{n}(X_i - \bar{X})^2}\sqrt{\sum_{i=1}^{n}(Y_i - \bar{Y})^2}} \tag{13}$$

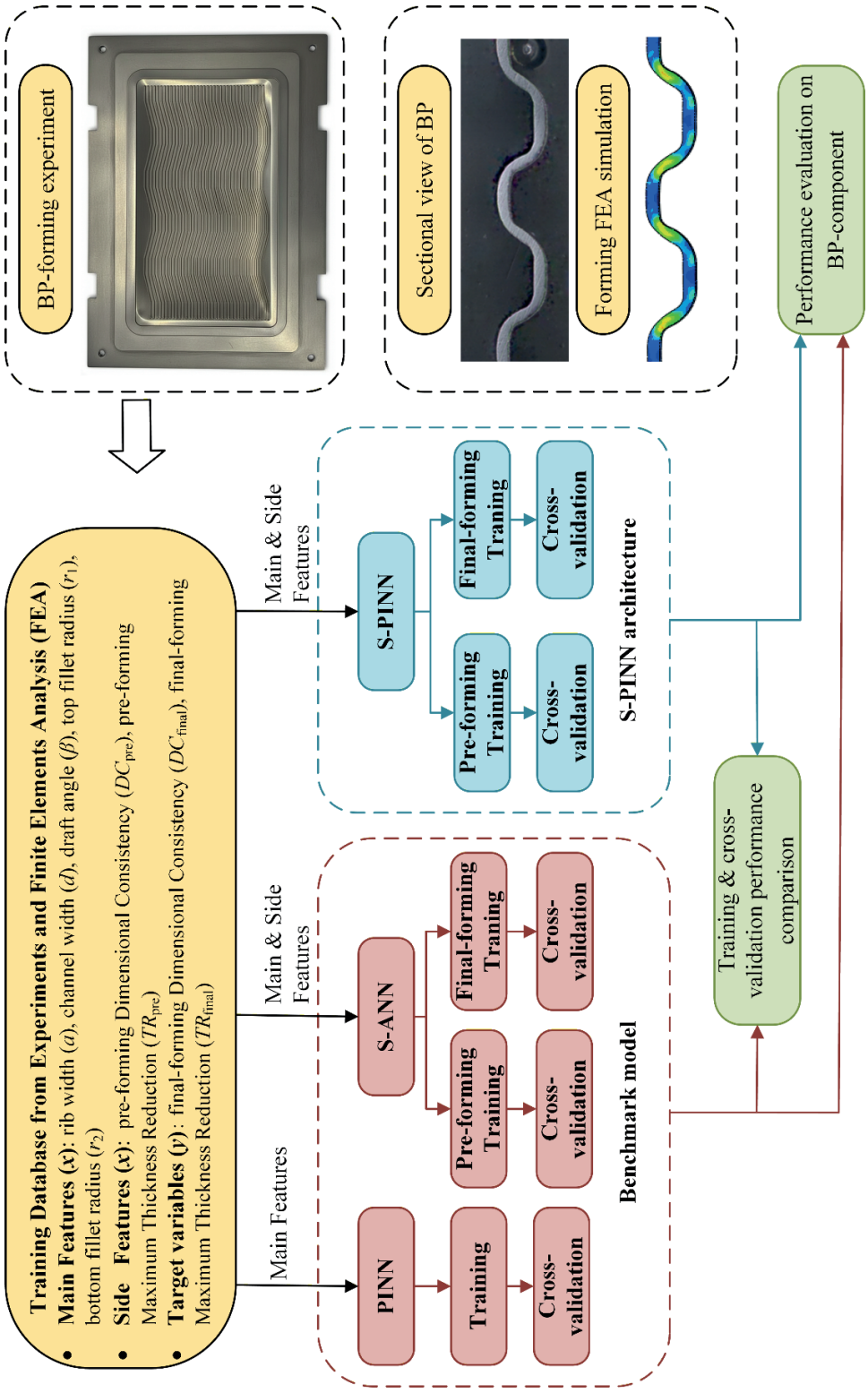

Fig. 5. Schematic diagram of the proposed machine learning framework

The Pearson correlation coefficient reflects the strength of the linear correlation between two variables; the larger the absolute value of r, the stronger the correlation. When $r > 0$, the two variables are positively correlated; when $r < 0$, they are negatively correlated; when $r = 0$, the variables are not linearly correlated but may exhibit other forms of correlation, such as a curved relationship; when $r = 1$ or -1, variables X and Y can be well described by a straight-line equation. After data preparation, the S-PINN model was trained using the Adam optimizer. Network weights were initialized with the Xavier (Glorot) scheme to ensure the gradients possessed effective initial variance.

2.6. Evaluation indicators

To rigorously assess the predictive performance and reliability of the proposed S-PINN framework, two complementary statistical metrics were employed: Root Mean Square Error (RMSE) and the Asymmetric Penalty Score (*Score*). RMSE, as a standard benchmark metric, is used to quantify the overall accuracy of the model, measuring the average magnitude of deviations between the predicted values ($\hat{y}_i$) and the true values (y_i) obtained from the FEA. The specific expression is shown in Eq. (14) (Hodson, 2022):

$$\mathrm{RMSE} = \sqrt{\frac{1}{N}\sum_{i=1}^{N}(\hat{y}_i - y_i)^2} \tag{14}$$

The Score mechanism applies varying degrees of penalties to prediction errors: when the predicted value is too high, the error increases exponentially; when the predicted value is too low, the rate of error growth slows down (Winkler, 1994), as expressed in Eq. (15).

$$Score = \sum_{i=1}^{N}\begin{cases}\exp\left(-\dfrac{d_i}{a_1}\right)-1 & \text{if} \quad d_i < 0\\ \exp\left(\dfrac{d_i}{a_2}\right)-1 & \text{if} \quad d_i \geq 0\end{cases} \tag{15}$$

where: $d_i = \hat{y}_i - y_i$ – prediction error; a_1, a_2 – scaling constants that control the penalty weight.

By combining RMSE and *Score* metrics, the evaluation framework not only assesses model accuracy but also validates the reliability of model engineering.

3. Die geometry optimization for two-stage stamping based on S-PINN

3.1. Predictive performance and validation of the S-PINN model

Before training the sequential physical information neural network, a comprehensive statistical analysis was conducted using the Pearson correlation coefficient (PCC) to quantify the relationships between key die feature parameters. These parameters include the bottom fillet radius r_2, top fillet radius r_1, rib width a, groove width d, and draft angle β. The calculated PCC matrix is presented as a heatmap in Fig. 6.

This analysis reveals the correlations between different geometric characteristic parameters. The top fillet radius r_1 is negatively correlated with the channel width d, indicating that, under the constraint of a fixed flow channel period, an increase in the top radius essentially limits the available width at the flat bottom of the channel. In addition, the rib width a show a significant negative correlation with the top fillet r_1. These complex nonlinear dependencies highlight the infeasibility of optimizing a single parameter in isolation, necessitating a multivariable optimization approach.

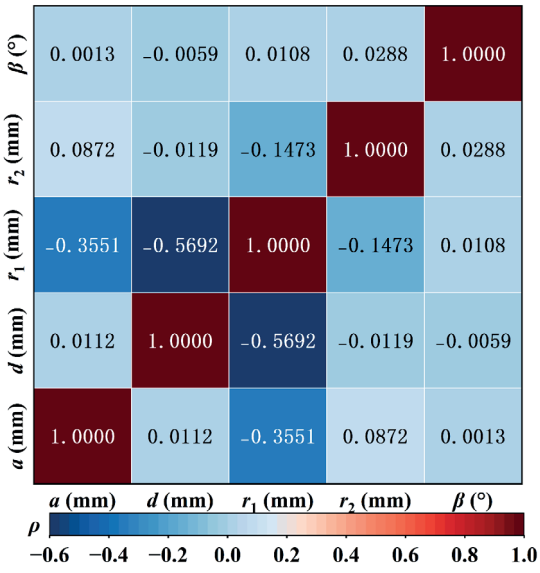

Fig. 6. Pearson correlation coefficient heatmap of die geometric parameters

The S-PINN framework was trained using the Adam optimizer for over 8,000 iterations with learning rates ranging from 1×10^{-5} to 1×10^{-2}. The loss function consists of both data loss and physics residual loss. As shown in the convergence curve in Fig. 7a, the total

loss exhibits a sharp decline over the first 2,000 epochs. This significant reduction mainly results from the rapid decrease in the data loss term. Fig. 7b displays the evolution of each loss component. The physics loss, by penalizing plastic accumulation behavior, steadily converges toward nearly zero. This stable convergence indicates that the S-PINN architecture has successfully learned to simulate the two-stage stamping process, memorizing the training data while also grasping the fundamental rules of plastic accumulation.

To evaluate the predictive capability of the trained S-PINN model, its prediction results were compared with high-fidelity FEA reference values. The comparison covered two metrics: DC_{final} and TR_{final}, as shown in Fig. 8. The scatter plot clearly shows that the predicted values closely align with the ideal diagonal line $y = x$. Specifically, the R^2 value for the DC prediction reached 0.9774, and the R^2 value for the TR prediction reached 0.9516. The high correlation coefficients of the two target variables in the S-PINN model fully validate its prediction accuracy.

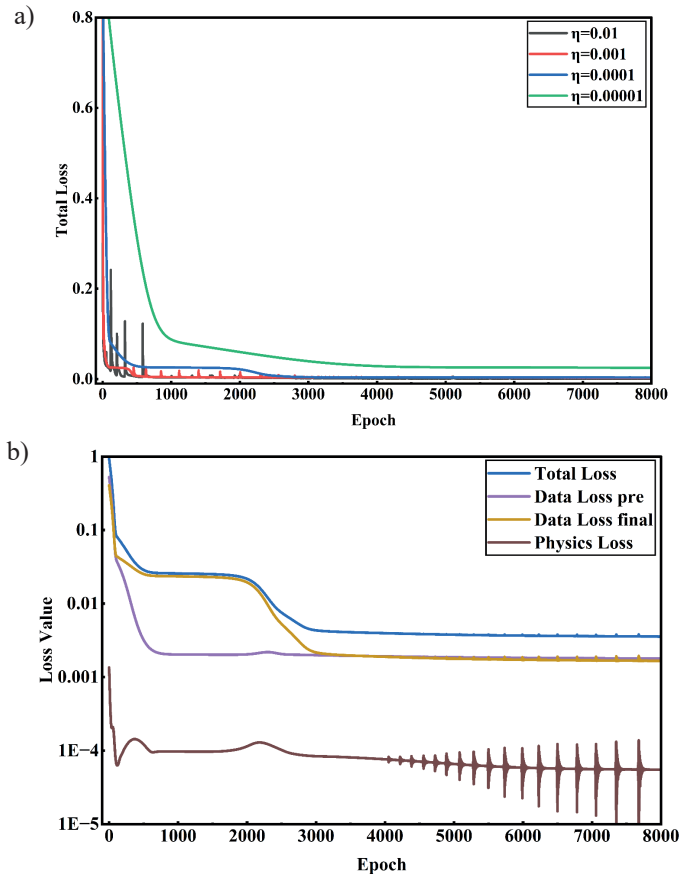

Fig. 7. Training convergence and loss analysis of the S-PINN model: a) effect of different initial learning rates (η) on the total loss convergence; b) evolution of the loss components during the training process

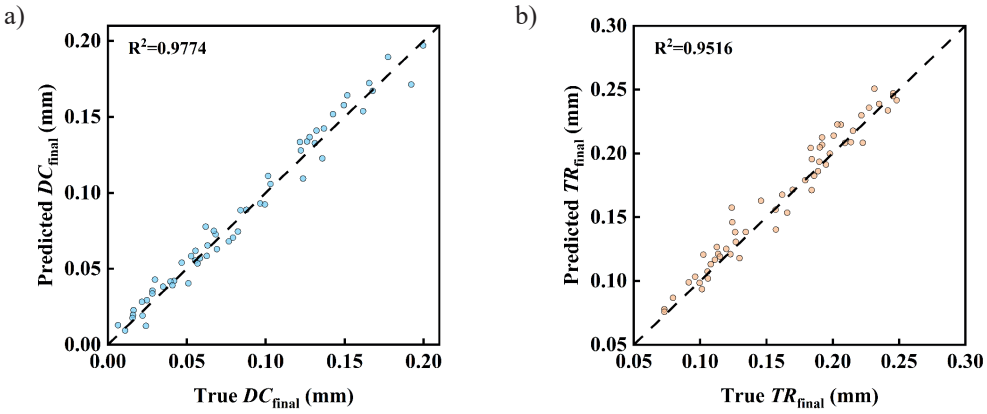

Fig. 8. The plots compare the truth values against the S-PINN predictions for: a) the final dimensional consistency (DC_{final}); b) the final thinning rate (TR_{final}); the dashed black lines represent the $y = x$ fit

3.2. Cross-validation

To evaluate the predictive robustness of the proposed computational framework, cross-validation was conducted across five architectures: S-ANN(Pre), S-PINN(Pre), S-ANN, standard PINN, and S-PINN. Fig. 9 presents the mean percentage errors alongside their corresponding standard deviations for both the training and validation datasets. As illustrated in Fig. 9a, the sequential architectures effectively capture the error propagation inherent in the two-stage stamping process. Predictably, both S-PINN and S-ANN yielded higher errors in the final forming stage compared to the pre-forming stage, reflecting the cumulative complexity of the deformation. Specifically, the dimensional consistency (*DC*) errors for S-PINN increased from 6.63% ±0.27% (training) and 7.79% ±0.79% (validation) in the pre-forming phase to 14.31% ±0.69% and 16.19% ±1.58% in the final phase. Similarly, S-ANN exhibited a comparable error accumulation, escalating from 5.04% ±0.16% and 6.31% ±0.51% to 21.65% ±0.78% and 26.41% ±1.97%. Despite this cumulative complexity, S-PINN demonstrated superior predictive fidelity for the final *DC*. By explicitly modeling the intermediate pre-form state and imposing physical constraints, S-PINN reduced the *DC* validation error by approximately 33.90% relative to S-ANN and 73.80% relative to the standard PINN. Furthermore, paired *t*-tests confirmed that these accuracy improvements by S-PINN are statistically highly significant (indicated by *** for $p < 0.001$ in Fig. 9a) when compared to both baseline models. Conversely, as depicted in Fig. 9b, the prediction errors for the final thickness reduction (*TR*) rate remained largely uniform across all architectures. Statistical analysis via paired *t*-tests revealed no significant differences (labeled as "ns") among the models for *TR* prediction. This indicates that *TR* prediction represents a lower-complexity task where baseline networks readily approach the performance ceiling. Nevertheless, the physics-constrained models (PINN and S-PINN) yielded noticeably narrower error bars, indicating enhanced predictive stability and reduced variance.

Overall, S-PINN exhibited the narrowest generalization gap between the training and validation sets, demonstrating robust resistance to both underfitting and overfitting. In contrast, standard PINN and S-ANN displayed slight overfitting tendencies, underscoring the necessity of coupling a sequential network topology with physical law constraints to accurately model complex, multi-stage forming processes.

To quantify the overall advantages of physical information and sequence structure, S-PINN was evaluated against two other models using comparative metrics. Fig. 10 demonstrates that, as assessed by RMSE and *Score*, S-PINN achieved reductions of 54.40% and 68.20% in size consistency prediction compared to the S-ANN baseline model, while *TR* prediction decreased by 4.50% and 9.30%. Compared to the standard PINN model, S-PINN achieved reductions of 66.60% and 81.90% in *DC* prediction, along with decreases of 0.90% and 4.10% in *TR* prediction.

S-PINN demonstrates superior predictive capability for *TR* compared to the other two models, while the prediction values among different models for *TR* show minimal variation. Although RMSE and *Score* evaluations show similar trends across models, the S-PINN model demonstrates greater advantages under the *Score* evaluation system. *Score* evaluation exhibits exponential error increases when predictions are excessively high, indicating that the other two models overestimate *DC* compared to S-PINN.

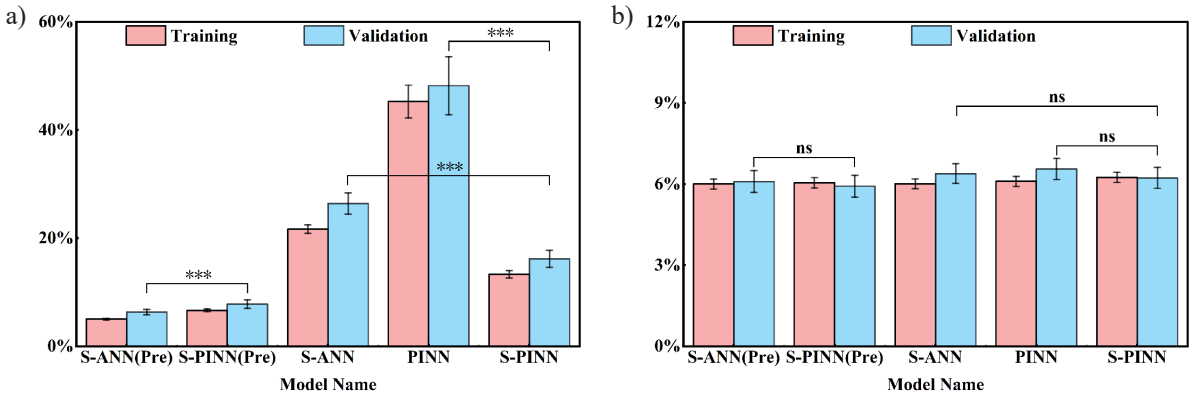

Fig. 9. Average percentage errors and standard deviations of: a) dimensional consistency (% error) [mm]; b) thinning rate for training and validation sets (% error)

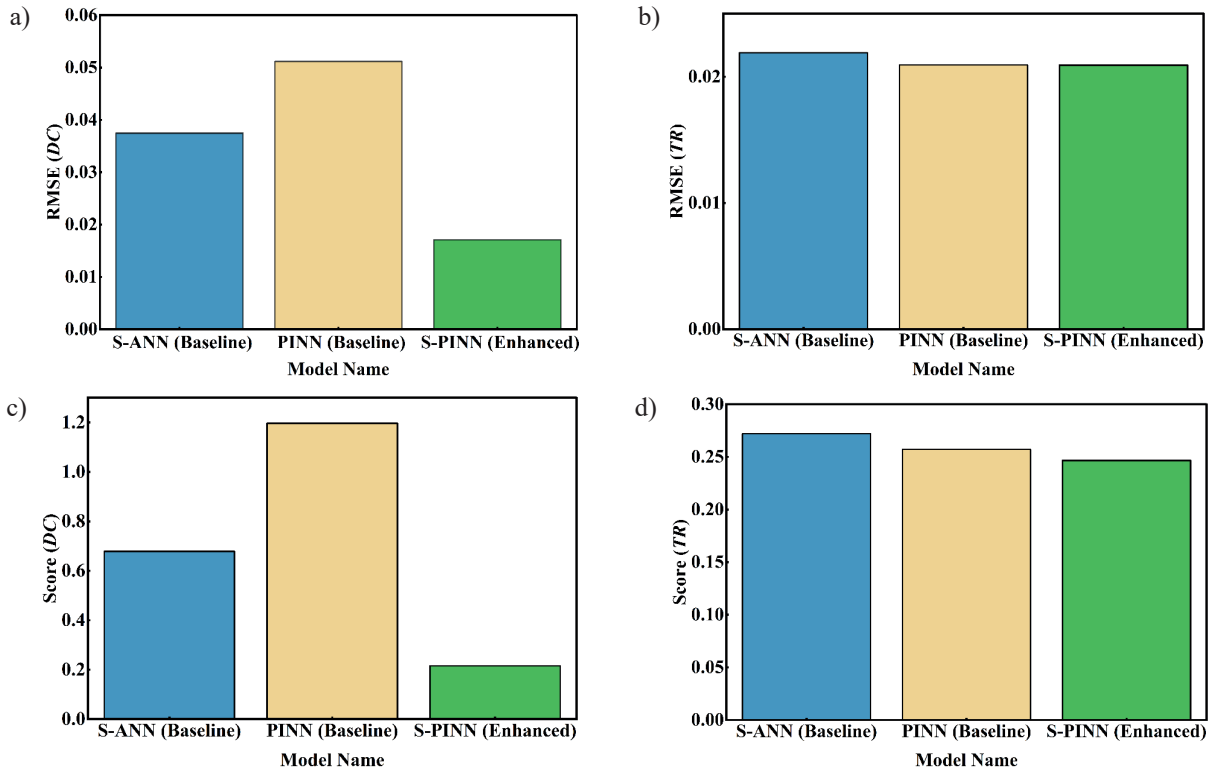

Fig. 10. Quantitative performance comparison among the S-ANN, PINN, and S-PINN models: a) the evaluation indicators include RMSE for dimensional consistency; b) RMSE for thinning rate; c) the *Score* for dimensional consistency; d) the *Score* for thinning rate

4. Discussion

This study establishes that sequential architectures offer distinct advantages over conventional single-layer neural networks when simulating two-stage stamping processes. Furthermore, the integration of primary physical constraints significantly enhances the predictive accuracy of the model. While standard, purely data-driven artificial neural networks can successfully map statistical correlations within localized training datasets, they inherently fail to capture the underlying physical causality of plastic deformation. When faced with die geometry inputs beyond the training envelope, the interpolation prediction accuracy of standard S-ANN decreases significantly. S-PINN sequentially decomposes the entire two-stage stamping process and introduces a monotonic residual term into the loss function. By incorporating the irreversibility of plastic damage, the model is able to learn the logical relationships between forming stages while fully accounting for the influence of the preforming process on the final forming state.

Beyond verifying predictive accuracy, these results provide critical guidance for optimizing die geometries, successfully locating the precise geometric balance point by mapping the Pareto optimal compromise space. As illustrated in Fig. 11 and 12, the 3D response surfaces predicted by the S-PINN clearly reveal the complex, highly coupled interactions that the five die geometric parameters exert on both the final thinning rate (TR_{final}) and dimensional consistency (DC_{final}). To achieve optimal die design, the well-trained S-PINN was seamlessly integrated into the NSGA-II algorithm to serve as a high-fidelity fitness evaluation function, effectively replacing traditionally time-consuming finite element iterative calculations. Through systematic reproduction, crossover, and mutation operations, the NSGA-II algorithm generated the Pareto Front depicted in Fig. 13. By comprehensively considering the coupled effects of *DC* and *TR*, the best combination of mold parameters is obtained as follows: rib width a = 0.3037 mm, groove width d = 0.3005 mm, top fillet radius r_1 = 0.1000 mm, lower fillet radius r_2 = 0.1000 mm, and draft angle β = 60.9595°. Utilizing this specific parameter configuration ensures the highest forming quality for the final titanium sheet.

To validate the practical reliability of this optimization framework, a new high-fidelity FEM simulation was executed using the derived optimal parameters (Fig. 14). The simulation results confirmed that the FEM outputs align closely with the optimal forming quality predicted by the S-PINN, thereby corroborating the practical validity of the proposed framework.

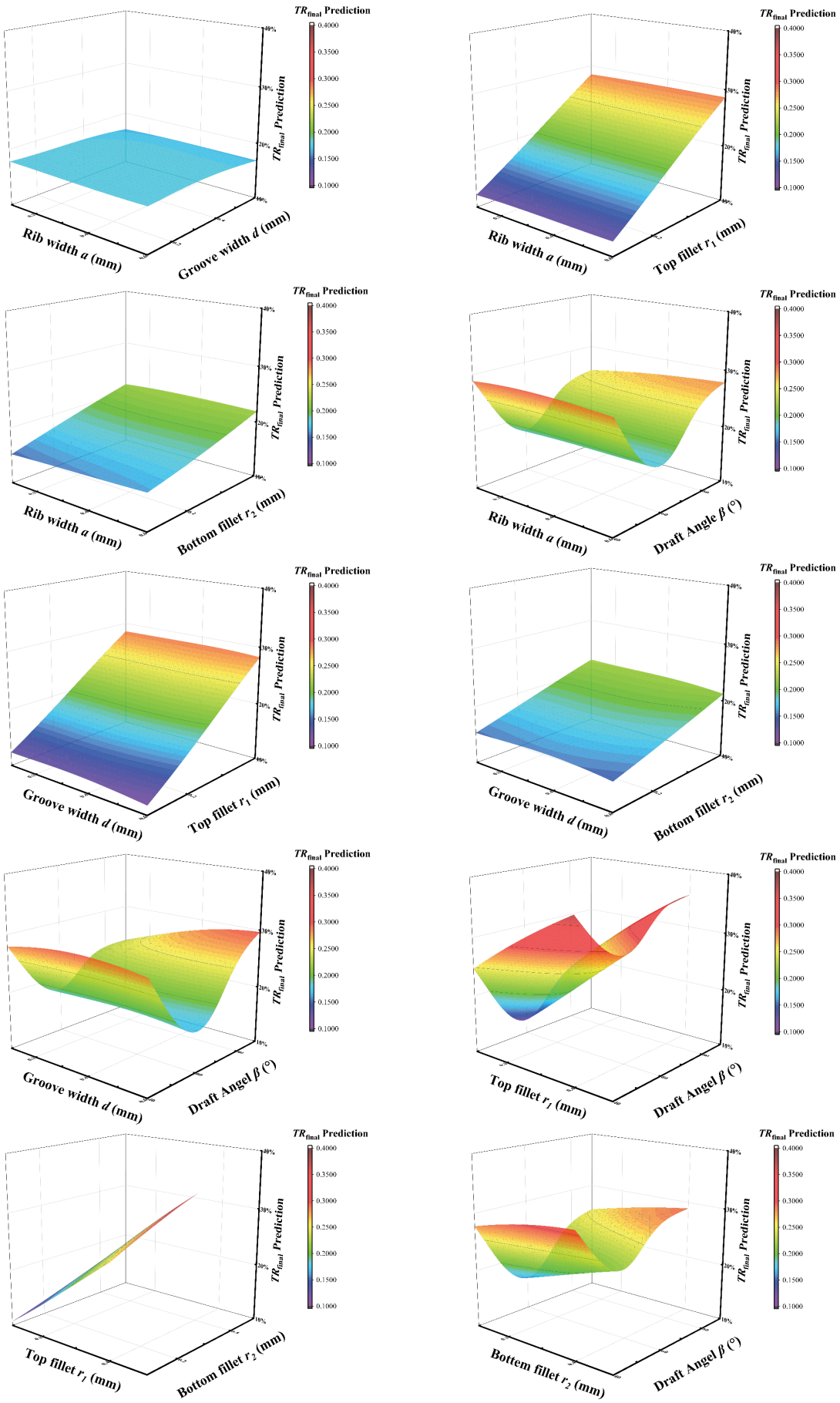

Fig. 11. Three-dimensional response surface of the final thinning rate (TR_{final}) predicted by S-PINN

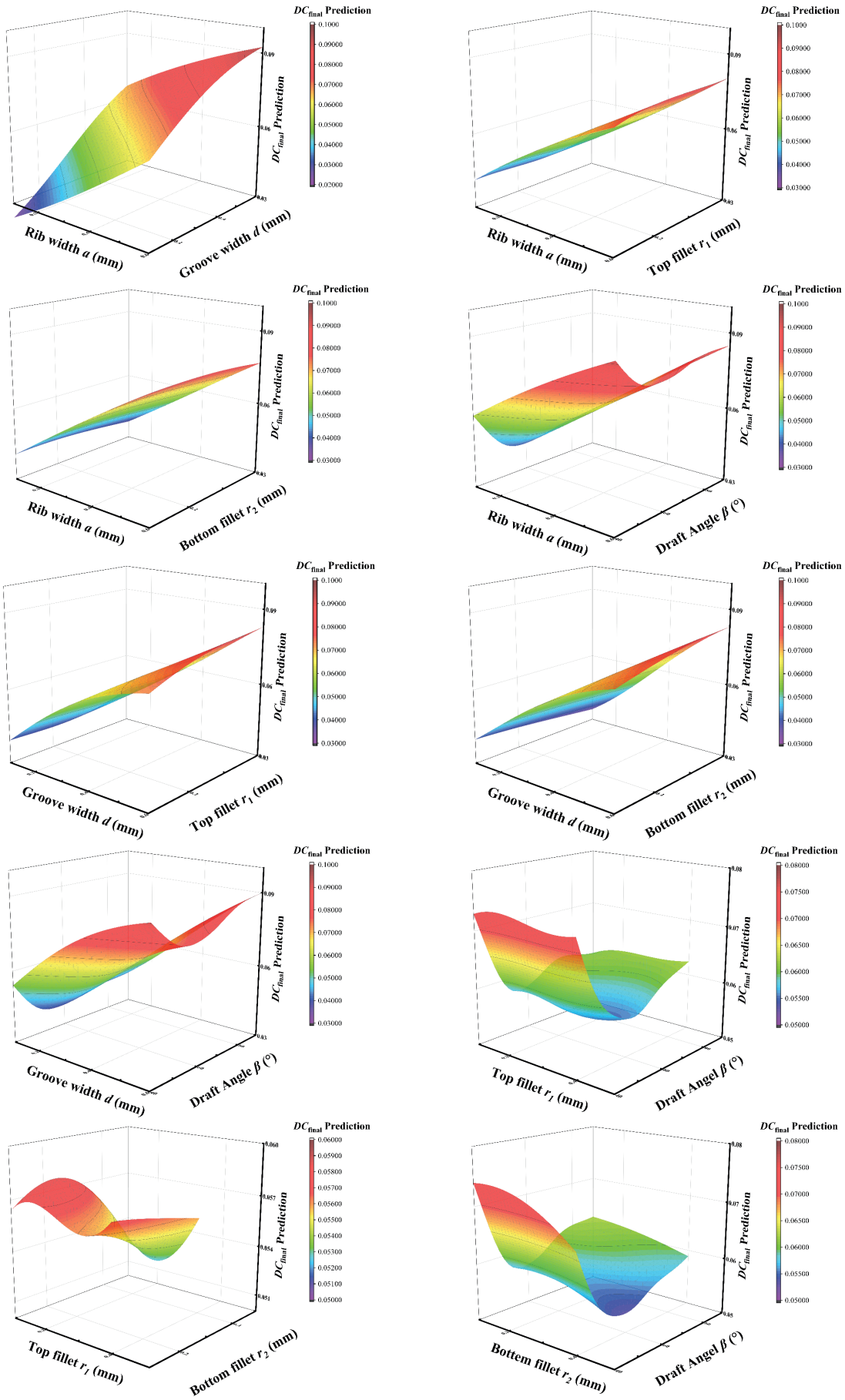

Fig. 12. Three-dimensional response surface of the final dimensional consistency (DC_{final}) predicted by S-PINN

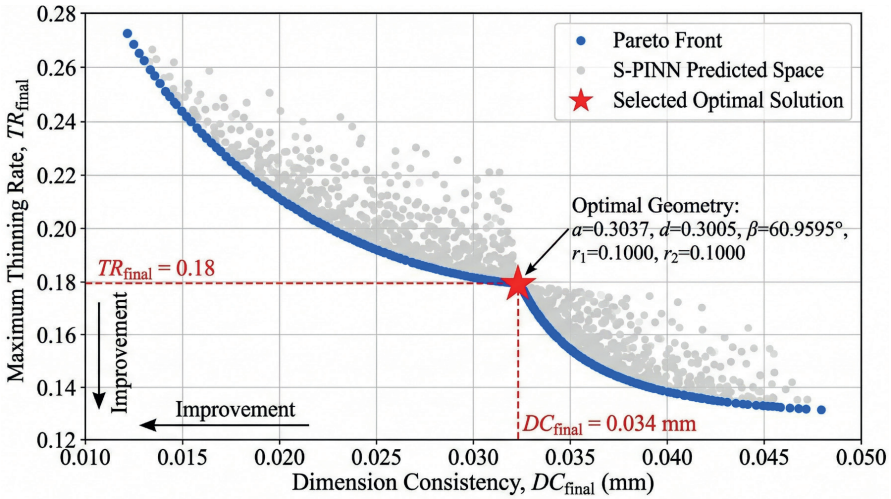

Fig. 13. Pareto Optimal Front for sheet forming Multi-objective Optimization

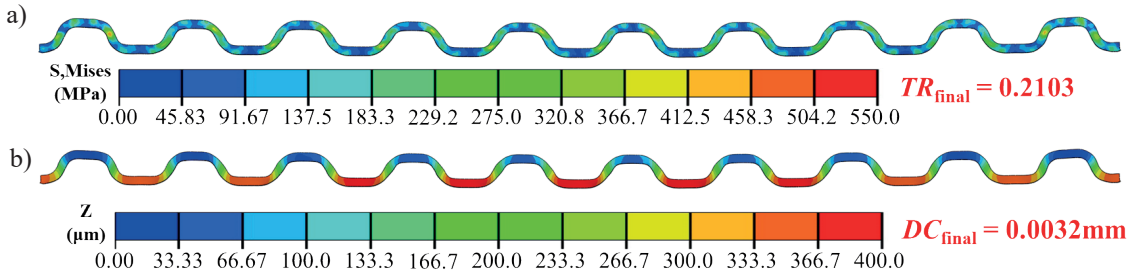

Fig. 14. Contour plots of the flow channel cross-section under optimal process parameters: a) von Mises stress distribution [MPa]; b) thickness-direction distribution

While the S-PINN optimization framework demonstrates clear success and industrial applicability, it is necessary to acknowledge its current analytical limitations, particularly regarding the potential for further improving the predictive accuracy of the thinning rate. These limitations likely stem from the model's explicit assumption that the quasi-static forming process occurs strictly at room temperature, deliberately ignoring the potential strain rate sensitivity and complex tribological changes during the two-stage stamping process, including the frequent dynamic coefficient of friction. Future research will focus on seamlessly integrating dynamic friction models into physical loss functions and extending the computational framework to cover complex high-temperature forming conditions, which is expected to significantly improve the ultimate forming performance of ultra-thin metal bipolar plates for next-generation proton exchange membrane fuel cells.

5. Conclusions

This study proposes and validates a novel Sequence Physics-Informed Neural Network (S-PINN) framework for optimizing two-stage stamping dies of ultra-thin titanium bipolar plates. By integrating the physical laws of material deformation into the neural network, it effectively addresses the limitations of traditional neural networks. The main conclusions are summarized as follows:

1. S-PINN uses a sequential structure to represent the two-stage stamping process of ultra-thin titanium sheets. Through monotonic residuals, it ensures that $TR_{final} \geq TR_{pre}$, explicitly enforcing the irreversible plastic damage law, reflecting the accumulation of plastic deformation of the material during the forming process.
2. The S-PINN model demonstrates outstanding predictive accuracy for both the final dimensional consistency (*DC*) and the final thinning rate (*TR*). This performance was quantitatively validated against true values, achieving an R^2 value of 0.9774 for *DC* and 0.9516 for *TR*.
3. The sequential architecture of neural networks can effectively capture multi-stage manufacturing processes. Introducing physical information constraints further improves the accuracy. Specifically for *DC* prediction, S-PINN improves by 33.9% compared to S-ANN and by 73.8% compared to the PINN model.

4. By seamlessly integrating the trained S-PINN model with the NSGA-II algorithm, the proposed framework successfully mapped the Pareto optimal compromise space, effectively replacing time-consuming finite element iterations. This approach identified the precise optimal die geometry (a = 0.3037 mm, d = 0.3005 mm, r_1 = 0.1000 mm, r_2 = 0.1000 mm, β = 60.9595°) to navigate the complex coupled effects of dimensional consistency and thinning rate, confirming its practical industrial viability.

Declaration of competing interest

The authors declare that they have no known competing financial interests or personal relationships that could have appeared to influence the work reported in this paper.

Acknowledgments

The authors would like to acknowledge the financial support from the National Key Research and Development Program of China (No. 2022YFB4003503).

CRediT authorship contribution statement

Zijie Ke: writing – original draft, visualization, software, methodology, validation, formal analysis, data curation; Yiwen Huang: data curation, methodology; Ziqiang Guo: data curation, methodology; Yao Xiao: writing – review & editing, methodology, investigation, formal analysis, data curation, conceptualization, funding acquisition; Zeran Hou: writing – review & editing, methodology, investigation, formal analysis, data curation, conceptualization; Junying Min: writing – review & editing, supervision, project administration.

References

Alhalaybeh, T. S., Muhamaiti, Y., Shang, H., Zhou, L., Liang, X., & Lou, Y. (2026). Artificial neural network based stamping process design for three-point bending. *Acta Mechanica Sinica*, *42*(3), 424895. https://doi.org/10.1007/s10409-025-24895-x

Asuero, A. G., Sayago, A., & González, A. G. (2006). The correlation coefficient: An overview. *Critical Reviews in Analytical Chemistry*, *36*(1), 41–59. https://doi.org/10.1080/10408340500526766

Bajda, S., & Krzyzanowski, M. (2019). Modelling aspects of laser cladding of bioactive glass coatings on ultrafine-grained titanium substrates. *Computer Methods in Materials Science*, *19*(3), 138–149. https://doi.org/10.7494/cmms.2019.3.0637

Benesty, J., Chen, J., Huang, Y., & Cohen, I. (2009). Pearson correlation coefficient. In *Noise Reduction in Speech Processing* (pp. 1–4). Springer, Berlin, Heidelberg. https://doi.org/10.1007/978-3-642-00296-0_5

Bezerra, M. A., Santelli, R. E., Oliveira, E. P., Villar, L. S., & Escaleira, L. A. (2008). Response surface methodology (RSM) as a tool for optimization in analytical chemistry. *Talanta*, *76*(5), 965–977. https://doi.org/10.1016/j.talanta.2008.05.019

Bong, H. J., Lee, J., Kim, J. H., Barlat, F., & Lee, M.-G. (2017). Two-stage forming approach for manufacturing ferritic stainless steel bipolar plates in PEM fuel cell: Experiments and numerical simulations. *International Journal of Hydrogen Energy*, *42*(10), 6965–6977. https://doi.org/10.1016/j.ijhydene.2016.12.094

Daud, W. R. W., Rosli, R. E., Majlan, E. H., Hamid, S. A. A., Mohamed, R., & Husaini, T. (2017). PEM fuel cell system control: A review. *Renewable Energy*, *113*, 620–638. https://doi.org/10.1016/j.renene.2017.06.027

Fan, E. (2000). Extended tanh-function method and its applications to nonlinear equations. *Physics Letters A*, *277*(4–5), 212–218. https://doi.org/10.1016/s0375-9601(00)00725-8

Guo, N., Zhang, X., Hou, Z., Wang, W., Yang, D., Min, J., Ming, P., & Zhang, C. (2023). Hot stamping of ultra-thin stainless steel sheets for bipolar plates. *Journal of Materials Processing Technology*, *317*, 117987. https://doi.org/10.1016/j.jmatprotec.2023.117987

Haghighat, E., Raissi, M., Moure, A., Gomez, H., & Juanes, R. (2021). A physics-informed deep learning framework for inversion and surrogate modeling in solid mechanics. *Computer Methods in Applied Mechanics and Engineering*, *379*, 113741. https://doi.org/10.1016/j.cma.2021.113741

Han, Z.-H., & Zhang, K.-S. (2012). 17: Surrogate-based optimization. In O. Roeva (Ed.), *Real-World Applications of Genetic Algorithms* (pp. 343–362). InTech. https://doi.org/10.5772/36125

Henderi, H., Wahyuningsih, T., & Rahwanto, E. (2021). Comparison of Min-Max normalization and Z-Score Normalization in the K-nearest neighbor (kNN) Algorithm to Test the Accuracy of Types of Breast Cancer. *International Journal of Informatics and Information Systems*, *4*(1), 13–20. https://doi.org/10.47738/ijiis.v4i1.73

Heras, N., de las, Roberts, E. P. L., Langton, R., & Hodgson, D. R. (2009). A review of metal separator plate materials suitable for automotive PEM fuel cells. *Energy & Environmental Science*, *2*(2), 206–214. https://doi.org/10.1039/B813231N

Hodson, T. O. (2022). Root mean square error (RMSE) or mean absolute error (MAE): When to use them or not. *Geoscientific Model Development Discussions*, *15*, 5481–5487. https://doi.org/10.5194/gmd-15-5481-2022

Karniadakis, G. E., Kevrekidis, I. G., Lu, L., Perdikaris, P., Wang, S., & Yang, L. (2021). Physics-informed machine learning. *Nature Reviews Physics*. https://doi.org/10.1038/s42254-021-00314-5

Lacki, P., Derlatka, A., Lacki, M., & Lachs, K. (2026). A Digital Twin for temperature prediction in the laser hardening process of NC10 steel. *Computer Methods in Materials Science*, *26*(1), 5–22. https://doi.org/10.7494/cmms.2026.1.1023

Lin, K., Qiao, J., Shi, K., Dong, W., & Gu, D. (2023). Laser powder bed fusion of micro-channels for the application of proton exchange membrane fuel cell bipolar plates. *CIRP Journal of Manufacturing Science and Technology*, *43*, 193–204. https://doi.org/10.1016/j.cirpj.2023.01.007

Modanloo, V., Jang, S., Lee, T., & Quagliato, L. (2025). Gradient Enhanced-Expert Informed Neural Network (GE-EINN) for forming depth prediction from a small-scale metal stamping dataset. *Journal of Manufacturing Processes*, *140*, 224–240. https://doi.org/10.1016/j.jmapro.2025.02.052

Oliver, M. A., & Webster, R. (1990). Kriging: a method of interpolation for geographical information systems. *International Journal of Geographical Information System*, *4*(3), 313–332. https://doi.org/10.1080/02693799008941549

Raissi, M., Perdikaris, P., & Karniadakis, G. E. (2019). Physics-informed neural networks: A deep learning framework for solving forward and inverse problems involving nonlinear partial differential equations. *Journal of Computational Physics*, *378*, 686–707. https://doi.org/10.1016/j.jcp.2018.10.045

Song, Y., Zhang, C., Ling, C. Y., Han, M., Yong, R.-Y., Sun, D., & Chen, J. (2020). Review on current research of materials, fabrication and application for bipolar plate in proton exchange membrane fuel cell. *International Journal of Hydrogen Energy*, *45*(54), 29832–29847. https://doi.org/10.1016/j.ijhydene.2019.07.231

Winkler, R. L. (1994). Evaluating probabilities: Asymmetric scoring rules. *Management Science*, *40*(11), 1395–1405. https://doi.org/10.1287/mnsc.40.11.1395

Xiao, W., Cai, H., Lu, W., Li, Y., Zheng, K., & Wu, Y. (2022). Multi-objective optimization with automatic simulation for partition temperature control in aluminum hot stamping process. *Structural and Multidisciplinary Optimization*, *65*(3), 84. https://doi.org/10.1007/s00158-022-03190-4

Yan, Y., Wang, H., & Li, Q. (2015). The inverse parameter identification of Hill 48 yield criterion and its verification in press bending and roll forming process simulations. *Journal of Manufacturing Processes*, *20*(1), 46–53. https://doi.org/10.1016/j.jmapro.2015.09.009

Yang, K.-T. (2008). Artificial neural networks (ANNs): a new paradigm for thermal science and engineering. *Journal of Heat Transfer*, *130*(9). https://doi.org/10.1115/1.2944238

Zhang, H., Xu, C., Gao, T., Li, X., & Song, H. (2023). Identification of strain hardening behaviors in titanium alloys using tension tests and inverse finite element method. *Journal of Mechanical Science and Technology*, *37*(7), 093001. https://doi.org/10.1007/s12206-023-0625-0

Zhang, R., Xu, Z., Peng, L., Lai, X., & Fu, M. W. (2021). Modelling of ultra-thin steel sheet in two-stage tensile deformation considering strain path change and grain size effect and application in multi-stage microforming. *International Journal of Machine Tools and Manufacture*, *164*, 103713. https://doi.org/10.1016/j.ijmachtools.2021.103713

Zhong, Q., Hua, R., Wang, C., Cheng, L., Ma, Z., He, H., & Chen, F. (2023). Investigation on three-stage stamping of micro-channels with titanium ultra-thin sheet used for PEM fuel cell bipolar plates. *The International Journal of Advanced Manufacturing Technology*, *127*(3), 1377–1389. https://doi.org/10.1007/s00170-023-11618-4

Appendix A

Systematic experimental validation of the finite element model

To ensure the physical reliability of the dataset used for training the Sequential Physics-Informed Neural Network (S-PINN) and to guarantee the fidelity of the finite element method (FEM) simulations, a systematic experimental validation was conducted prior to surrogate modeling. This section details the comparative analysis between the numerical predictions and the physical two-stage stamping experiments.

Two-stage stamping experiments were conducted using 0.12 mm commercial pure titanium (CP-Ti) sheets. The die dimensions are listed in Tab. A.1. Following the complete two-stage forming and springback procedure, the resulting ultra-thin bipolar plate specimen was sectioned. The cross-sectional profile and localized thickness distribution were meticulously measured using a high-precision optical microscope. The reliability of the FEM model was assessed through both qualitative morphological alignment and quantitative dimensional metrics.

Table A.1. Geometric parameters of dies for pre- and final stamping forming

Geometric parameters of dies	Pre-forming	Final forming
a [mm]	0.25	0.29
d [mm]	0.25	0.35
r_1 [mm]	0.25	0.25
r_2 [mm]	0.13	0.13
β [°]	63	63

The cross-sectional profile predicted by the FEA and the experimental microscopic image are shown in Fig. A.1a. The numerical predictions demonstrated exceptional morphological agreement with the physical samples. Specifically, the model accurately captured the complex channel geometry, the localized bending severity at the top and bottom fillet radii, and the final springback deviations. As shown in Fig. A.1b, the thickness distribution along the cross-sectional arc length was extracted from both the experimental sample and the FEM model. The simulation successfully and precisely replicated the severe localized thinning occurring at the stress concentration zones near the die corner radii. Quantitative analysis revealed that the maximum deviation in the channel thickness between the experimental measurement and the FEM prediction was tightly maintained within 4.5%. As shown in Fig. A.1c, compared with the experimental data, the deviation between the simulated flow channel depth and the measured value was within 3 μm. The dimensional error of the final channel depth, which directly determines the dimensional conformance (*DC*), was strictly controlled within 3.2%.

The high degree of correlation between the experimental physical outcomes and the numerical simulations confirms that the formulated FEM model accurately captures the complex elastic-plastic deformation mechanisms and contact friction behaviors inherent in the two-stage stamping process. Consequently, the comprehensive dataset comprising 500 simulation cases generated via this validated FEM model is of high fidelity, providing a robust, scientifically rigorous, and credible ground truth for training the S-PINN optimization framework.

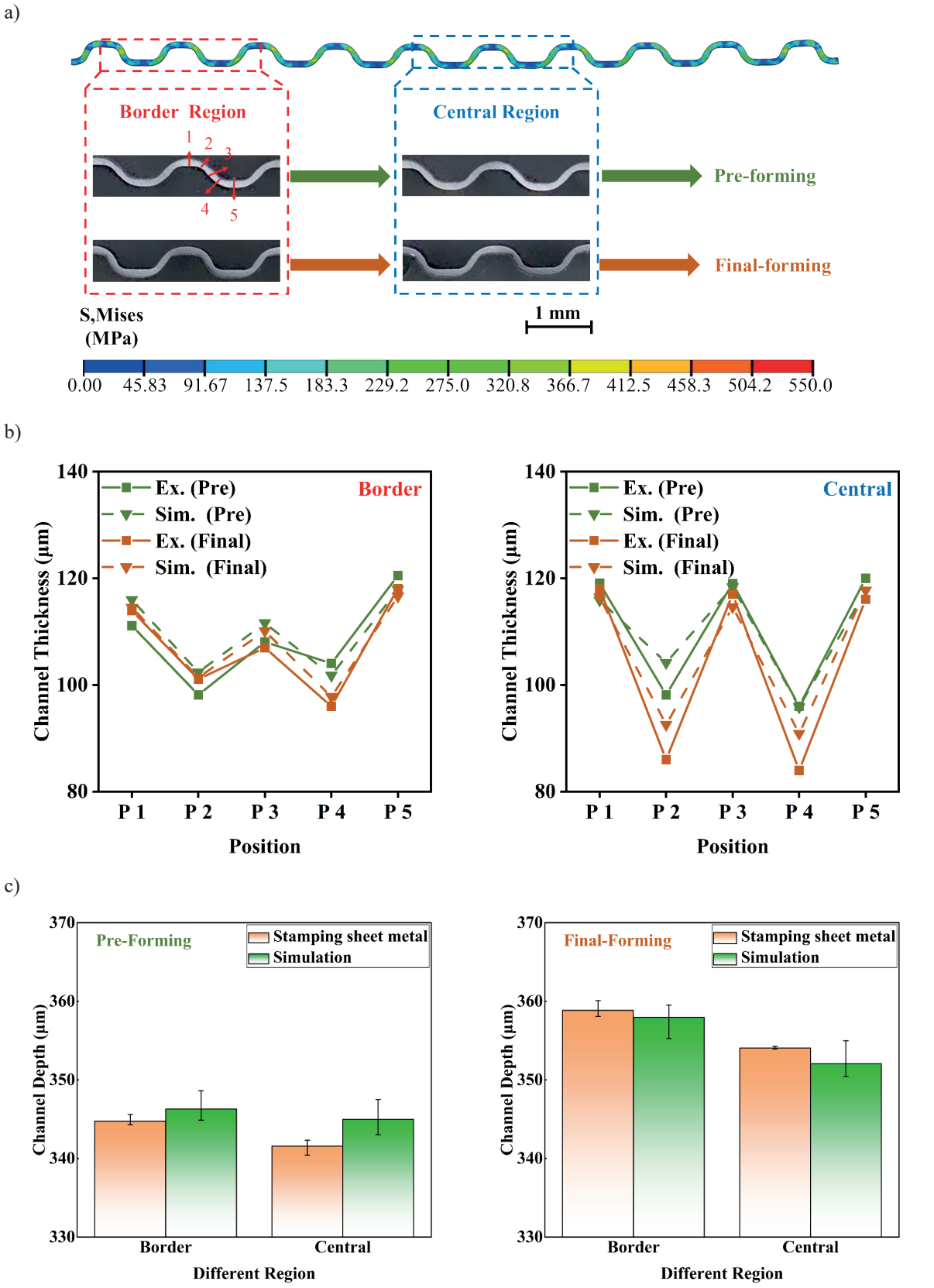

Fig. A.1. Experimental validation of the FEA model: a) comparison of the simulated and experimental cross-sectional profiles; b) channel thickness at different positions in the border and central regions; c) comparison between experimental and simulation results for the depth at the border and central regions of the flow channel in pre-formed and final-formed sheets